PNAS RESEARCH ARTICLE | CHEMISTRY

Scaling of quantum interference from single molecules to molecular cages and their monolayers

Xiaohui Xu[a,1], Juejun Wang[a,1], Nickel Blankevoort[b,1], Abdalghani Daaoub[b], Sara Sangtarash[b], Jie Shi[a], Chao Fang[a], Saisai Yuan[a], Lichuan Chen[a], Junyang Liu[a], Yang Yang[a,2], Hatef Sadeghi[b,2], and Wenjing Hong[a,2]

Edited by Michael Wasielewski, Northwestern University, Evanston, IL; received July 11, 2022; accepted October 11, 2022

The discovery of quantum interference (QI) is widely considered as an important advance in molecular electronics since it provides unique opportunities for achieving single-molecule devices with unprecedented performance. Although some pioneering studies suggested the presence of spin qubit coherence and QI in collective systems such as thin films, it remains unclear whether the QI can be transferred step-by-step from single molecules to different length scales, which hinders the application of QI in fabricating active molecular devices. Here, we found that QI can be transferred from a single molecule to their assemblies. We synthesized and investigated the charge transport through the molecular cages using 1,3-dipyridylbenzene (DPB) as a ligand block with a destructive quantum interference (DQI) effect and 2,5-dipyridylfuran (DPF) as a control building block with a constructive quantum interference (CQI) effect using both single-molecule break junction and large area junction techniques. Combined experiments and calculations revealed that both DQI and CQI had been transferred from the ligand blocks to the molecular cages and the monolayer thin film of the cages. Our work introduced QI effects from a ligand to the molecular cage comprising 732 atoms and even their monolayers, suggesting that the quantum interference could be scaled up within the phase-coherent distance.

single-molecule electronics | scanning tunneling microscope break junction | quantum interference | charge transport | flicker noise analysis

Significance

Quantum interference (QI) is one of the most important and general features of quantum systems. The advances of QI in molecular electronics provide unique opportunities for achieving single-molecule devices with unprecedented performance. Figuring out whether the QI can be transferred among the different length scales will facilitate the application of QI in fabricating active molecular devices. Here, we demonstrated experimentally that the QI was scaled up from a single molecule to the molecular cage and further to the thin film of the molecular cages. The conductance of one molecular cage constructed by ligand with constructive QI is 42 times that of another cage with destructive ligands. Our study paves the way for the application of QI-based electronic materials.

The quantum interference (QI) effect provides a unique opportunity to modulate single-molecule electron transport by the mechanism of phase-coherent tunneling (1–7), which offers great potential for the design of molecular electronic devices and materials with controllable electrical characteristics (8–11). The modulation mechanism of QI leads to single-molecule switches with high on–off ratios (12–14), organic dielectric material devices with low leakage current (15, 16), proof-of-principle single-molecule insulators (17), and vast applications in energy sciences (18, 19). Some pioneering works demonstrated the scaling of spin qubit coherence and the transference of QI from single-molecule to self-assembled monolayer films, even in the hybrid two-dimensional superlattices (8, 20–24), and QI effects were reserved as the molecule length increased (25). The largest molecular QI system that has been ever achieved is a benzothiadiazole-based 6-nm molecular wire, which was composed of 415 atoms (25). However, it is still unknown whether the QI can be transferred from the single-molecule scale to a larger and more complex molecular system.

The molecular cages provide prototype systems with atomically well-defined structures to investigate the scaling effect of QI (25–33). The molecular cages are constructed with organic ligands having hundreds of atoms, which offer opportunities to study whether these QI effects can transfer from organic linkers to their assembled structures, including molecular cages and monolayers of cages. The investigation of charge transport through molecular junctions, including the single-molecule junction, the single-assembly junction, and the large area junction of monolayer, provides opportunities to understand the evolution of QI along with different scales (34–36). Recent advances in scanning tunneling microscopy break junction (STM-BJ) and eutectic Ga-In (EGaIn) techniques provide opportunities to directly measure the conductance of single-ligand junctions (6, 37–39), single-cage junctions, and their monolayers, leading to the demonstration of how the QI transfers from ligands to their assemblies step-by-step.

In this work, we studied charge transport through single-ligand junctions and compared the results with those through the single-molecule cages (732 atoms) and their monolayers. The single-molecule conductance of two ligands, 1,3-dipyridylbenzene (DPB) and 2,5-dipyridylfuran (DPF), and their corresponding molecular cages, the DPB and DPF cages, were measured using the STM-BJ technique (Fig. 1*A*). It is also

Author affiliations: [a]State Key Laboratory of Physical Chemistry of Solid Surfaces, College of Chemistry and Chemical Engineering & Pen-Tung Sah Institute of Micro-Nano Science and Technology, IKKEM, Xiamen University, Xiamen 361005, China; and [b]Device Modelling Group, School of Engineering, University of Warwick, CV4 7AL Coventry, United Kingdom

Author contributions: Y.Y., H.S., and W.H. designed research; X.X., J.W., N.B., A.D., S.S., J.S., C.F., S.Y., L.C., and J.L. performed research; X.X., J.W., N.B., A.D., S.S., J.S., C.F., S.Y., L.C., J.L., Y.Y., H.S., and W.H. analyzed data; and X.X., Y.Y., and W.H. wrote the paper.

The authors declare no competing interest.

This article is a PNAS Direct Submission.

[1]X.X., J.W., and N.B. contributed equally to this work.

[2]To whom correspondence may be addressed. Email: yangyang@xmu.edu.cn or hatef.sadeghi@warwick.ac.uk or whong@xmu.edu.cn.

This article contains supporting information online at http://www.pnas.org/lookup/suppl/doi:10.1073/pnas.2211786119/-/DCSupplemental.

Published November 7, 2022.

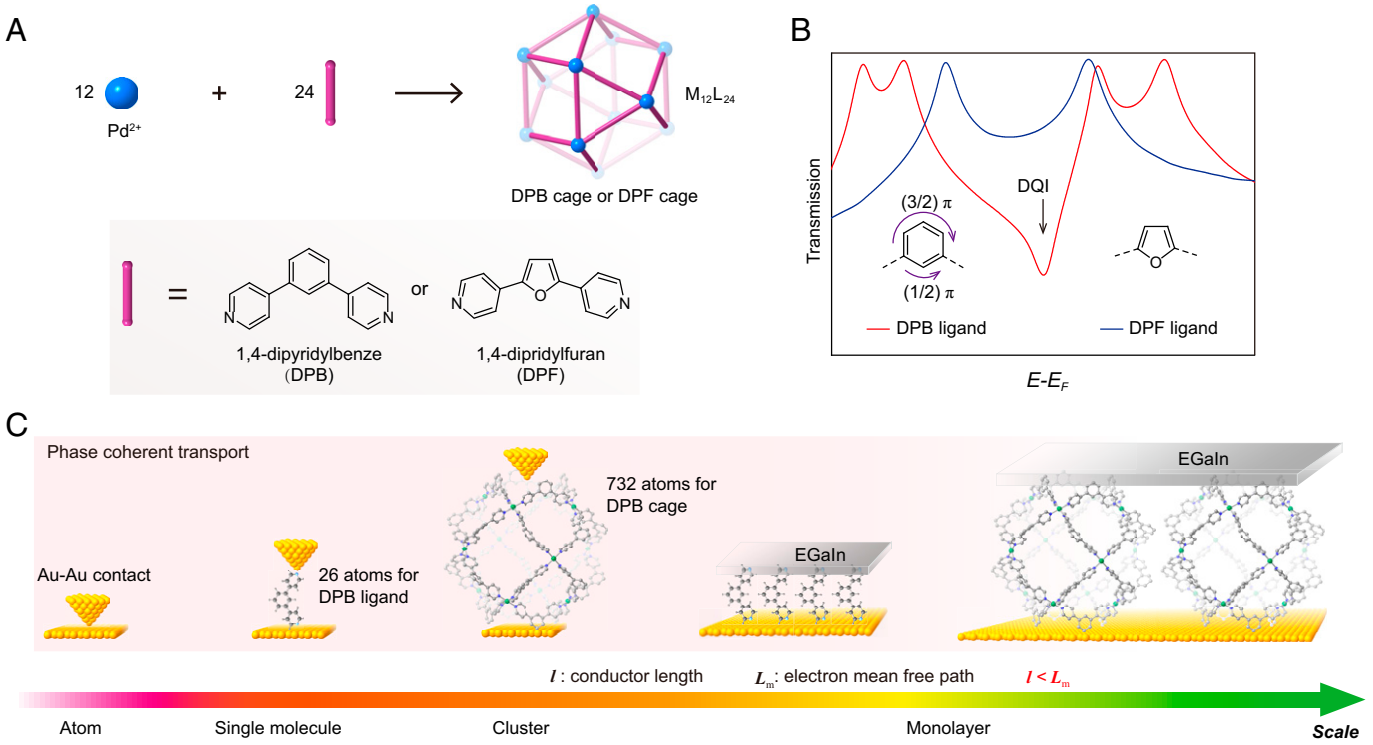

Fig. 1. Schematic evolution of quantum interference effect in the molecular junctions with length scales investigated using STM-BJ and EGaIn techniques. (*A*) The synthesis of $M_{12}L_{24}$ (M, metal; L, ligand) molecular cages. (*B*) Room temperature conductance versus electrodes Fermi energy obtained from tight-binding DFT for DPB and DPF ligands. The transmission curve (red) of DPB ligand shows sharp dip compares to that of DPF ligand (dark blue), indicating its DQI feature. (*C*) Schematic illustration for the conductance measurements of DPB ligand, DPF ligand, DPB cage, and DPF cage by STM-BJ and EGaIn techniques, respectively.

worth mentioning that the DPB cage constructed by 732 atoms was found to be the largest and the most complicated molecular system with QI effects in single-molecule junctions. The conductance of thin films formed by DPB, DPF ligands, and their corresponding molecular cages were characterized by the EGaIn technique, which showed a similar trend to that in the single-molecule junctions, suggesting that the QI reserves in thin films. Density functional theory (DFT) calculations reveal that the coupling between two adjacent Pd atoms gives rise to the electronic properties of an individual molecular cage. This Pd–Pd coupling was controlled by the corresponding QI effect in ligands and both can be transferred from ligands to the cages and even to the thin films. The results presented here show that the QI can transfer from a single ligand, to a single assembly of molecular cage, and even further to the thin film of molecular cages.

Results

Design and Synthesis of the Molecular Cages. To design the molecular systems with DQI, the transmission curves of single-molecule junctions with two ligands, DPB and DPF, are calculated first by using tight-binding DFT method (40), as shown in Fig. 1*B*. We found that the DPB ligand shows lower transmission than that of the DPF ligand, and the clear dip in the transmission of DPB suggests the presence of DQI in DPB. To further investigate whether the DQI in the DPB could be transferred to molecular cages, the two $M_{12}L_{24}$ (M, metal; L, ligand) molecular cages were synthesized based on the solvothermal reaction of Pd^{2+} with the two dipyridyl ligands (41) (Fig. 1*A* and *SI Appendix*, section S1) and the quantitative reactions were confirmed by both ^{1}H and ^{13}C nuclear magnetic resonance (NMR) spectroscopy (*SI Appendix*, Figs. S1–S4). In DPB cages, the relative positions of both ^{1}H and ^{13}C NMR signals were the same with DPB ligands, but the peaks were broadened and left-shifted (*SI Appendix*, Figs. S1 and S2). This finding suggests that the molecular cages were formed by the coordination between Pd^{2+} and DPB ligands, since previous reports demonstrated that the weakened anisotropy in liquid solution could be ascribed to the slow motion of large species (41, 42). The underlying structure of $M_{12}L_{24}$ cages is within high geometrical symmetry and can be described as polyhedral, in which the Pd^{2+} ions are regarded as vertices and the DPB or DPF ligands as edges. This polyhedral shape facilitates the orientation of cages on the Au substrates. In both DPB and DPF cages, the lowest unoccupied molecular orbital (LUMO) was mainly distributed around Pd atoms, which facilitate the contact between Pd atoms and the Au electrode to form stable single-cage junctions (*SI Appendix*, section S7).

Conductance Measurements for Single-Molecule Junctions. To investigate the charge transport through the ligands, the STM-BJ technique was employed to measure the conductance of the single-molecule junctions. A 0.1 V bias voltage was applied between the gold tip and the substrate for the conductance measurement, and typical individual conductance-displacement traces obtained showed distinct plateaus at different conductance ranges for all the samples (Fig. 2*B*). Each one-dimensional (1D) histogram is constructed from more than 2,000 individual conductance-displacement traces with no data selection (Fig. 2*C*). The Au–Au atomic point contact contributed to a sharp peak at 1 G_0 for each 1D histogram (43). The most probable conductance signals with Gaussian fitting are $10^{-4.80 \pm 0.2}$ G_0 (1.23 nS) for the DPB ligand and $10^{-3.84 \pm 0.2}$ G_0 (11.2 nS) for the DPF ligand. Two-dimensional (2D) conductance histograms against

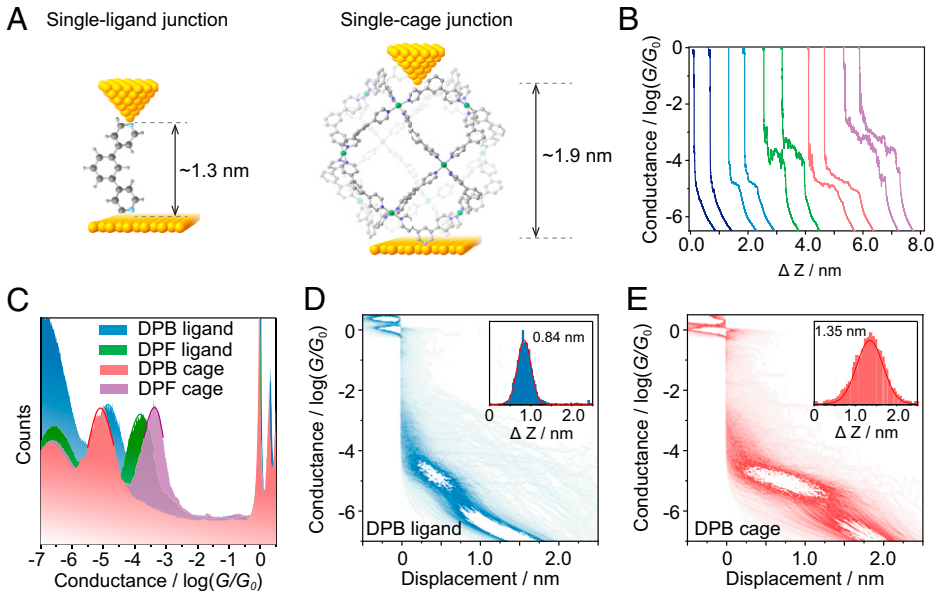

Fig. 2. The conductance measurements for single-molecule junctions composed of DPB ligand, DPF ligand, DPB cage, and DPF cage. (*A*) Illustration of single-molecule/cage junctions of DPB ligand, DPF ligand, DPB cage, and DPF cage. (*B*) Typical individual traces of different samples measured at 0.1 V: dark blue for blank, blue for DPB ligand, green for DPF ligand, pink for DPB cage and purple for DPF cage, respectively. (*C*) One dimensional single-molecule conductance histograms of DPB ligand, DPF ligand, DPB cage, and DPF cage measured at 0.1 V bias, respectively. (*D* and *E*) The corresponding 2D conductance histograms for DPB ligand and DPB cage in (*C*).

the relative distances of these samples were constructed by their individual conductance-displacement traces (Fig. 2*D* and *SI Appendix*, Fig. S6). These figures showed clear conductance intensity clouds, indicating that stable and reproducible single-molecule junctions were formed during the stretching cycles. The positions of these conductance clouds were consistent with the values in their 1D histograms. With the displacement distribution analysis of these molecular junctions, ∼0.8 nm for both ligands, we found the junction lengths in both ligands were ∼1.3 nm after the calibration of an additional 0.5 nm Au–Au snap back (44, 45). The single-molecule conductance of DPF ligand is approximately eight times higher than that of DPB ligand, showing the presence of DQI effects in DPB ligand (46, 47).

To determine if the DQI effects in the DPB ligand can be transferred to the molecular cages, STM-BJ was further employed to construct single-molecule junctions of the molecular cages. The single-molecule conductance measurement showed that the most probable conductance signals with Gaussian fitting are $10^{-4.97 \pm 0.2}$ G_0 (0.831 nS) for the DPB cage and $10^{-3.35 \pm 0.2}$ G_0 (34.6 nS) for DPF cage (Fig. 2*C*). The 2D conductance histograms showed clear intensity clouds, and the lengths of the single-cage junctions are ∼1.9 nm after accounting for the Au snap-back, suggesting that the electrodes bind to the cages via the coordinate configuration but not along the diameter of the cage (Fig. 2*E* and *SI Appendix*, Fig. S6). The conductance of the DPF cage is ∼41 times higher than that of the DPB cage with a similar charge transport distance. To further confirm the presence of quantum interference in the molecular cages, flicker noise analysis was carried out to reveal the mechanism of charge transport through single-molecule junctions (48). Previous reports demonstrated that this flicker noise analysis could generate power spectral density (PSD) spectra to determine whether the transport is through-space ($G^{2.0}$) or through-bond ($G^{1.0}$) (49, 50). For the single-ligand junctions, the PSD was scaled as $G^{1.8}$ for DPB ligand, while the value of DPF ligand was scaled as $G^{1.4}$ (Fig. 3 *A*–*D*). The results indicated DQI induced through-space mechanism in DPB ligand's charge transport pathways (51) (*SI Appendix*, Figs. S8–S11). In the molecular cages, the PSD was scaled to be $G^{1.3}$ for DPB cage, which is slightly larger than that of DPF cage ($G^{1.2}$), suggesting QI effects still exists in their molecular cages.

We carried out thermopower measurements for these molecular junctions to determine the relative position of Fermi energy by a home-built STM-BJ instrument equipped with thermopower modules (*SI Appendix*, Fig. S12) (52–56). The alignment of Fermi energy level of Au electrodes determines whether the electron transport in these molecules and molecular cages passed through the highest occupied molecular orbitals (HOMOs) or lowest unoccupied molecular orbitals (LUMOs). In a typical thermopower measurement, the Au substrate was heated by a Peltier device, and the stable temperature differences were created by a thermocouple mounted on the substrate with a feedback control circuit. The thermoelectric voltage (ΔV_{th}) of the entire single-molecule junction was recorded in each soft-contact break junction (*SI Appendix*, section S3). 1D histogram of the ΔV_{th} was constructed to give the average value by Gauss fitting at each temperature gradient to determine the thermopower. According to previous studies (54, 56), the Seebeck coefficient of a single-molecule junction can be calculated by the equation, $S_{junction} = S_{Cu} - (\Delta V_{th}/\Delta T)$, where S_{Cu} is the Seebeck coefficient of copper wire connected to the heated substrate. The copper wire contributes to the overall thermoelectric voltage and the value is 1.94 μV K^{-1} at 300 K. For DPB ligand, DPB cage, DPF ligand, and DPF cage, their Seebeck coefficients were all negative as obtained from the measured thermoelectric voltage as a function of temperature differences (Fig. 3 *E* and *F* and *SI Appendix*, Figs. S13 to S18), indicating the Fermi energy levels are close to the LUMO for all these four single-ligand/cage junctions. The DPB ligand with DQI effect has a smaller Seebeck coefficient than that of DPF, while the value of DPB cage is also smaller than DPF cage. The measured Seebeck coefficients of DPB ligand and DPB cage were smaller than those molecules without DQI effects (52, 55–57), again suggesting the presence of DQI effect in both junctions.

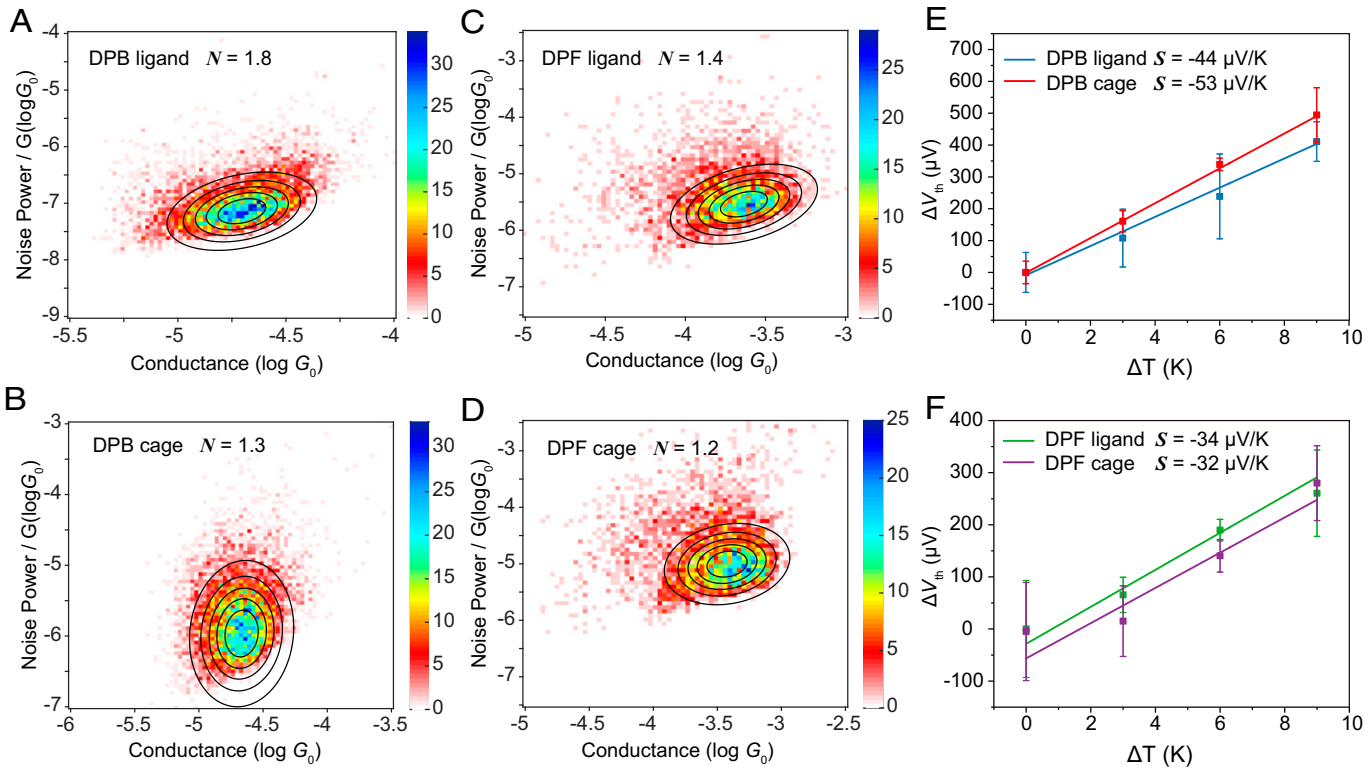

Fig. 3. The mechanism of charge transport through four different molecular junctions. (*A*–*D*) Two-dimensional histogram of normalized flicker noise power against average junction conductance for DPB ligand (*A*), DPB cage (*B*), DPF ligand (*C*), and DPF cage (*D*). (*E* and *F*) The Seebeck coefficients for single-molecule junctions fabricated based on DPB ligand (blue), DPB cage (red), DPF ligand (green), and DPF cage (purple), as obtained from the thermoelectric voltage as a function of temperature differences.

Conductance Measurements for Thin Films and Powders. To investigate whether the QI in DPB and DPF could scale up in the monolayer thin films, we measured the electrical characteristics of large-area molecular junctions of the ligands and their corresponding molecular cages using the EGaIn technique. These thin films were fabricated by immersing Au substrates into dimethyl sulfoxide (DMSO) solutions containing either the ligands or molecular cages, and their morphology was characterized by atomic force microscopy (58) (*SI Appendix*, section S4), indicating that the surfaces were homogenous and the relative roughness matched well with their respective molecular lengths. The conductance of these thin films was measured by putting them into contact with conical GaIn alloy tips with a home-built EGaIn instrument (59) (Fig. 4*A*). We collected many current density (*J*) curves of EGaIn/GaO_x//DPB/$Au^{A\text{-}DE}$ junctions (where "//" represents physisorption, "/" represents chemisorption, and

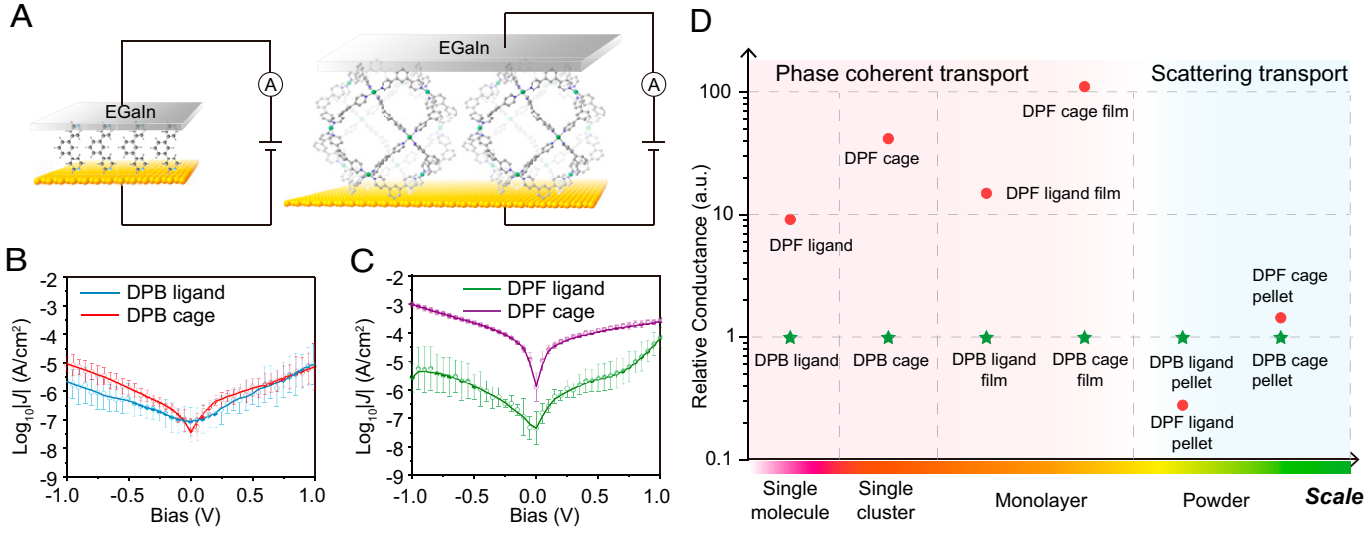

Fig. 4. Conductivity measurements in the molecular thin films of DPB ligand, DPF ligand, DPB cage, and DPF cage, compared to those measured at the macroscopic scale. (*A*) Schematic illustration of the conductance measurements for microscopic thin films. (*B* and *C*) The *J*(V) curves of the monolayer of DPB ligand, DPB cage, DPF ligand, and DPF cage measured using EGaIn top contacts. The error bars are the log-SDs of Gaussian fitting. (*D*) The green stars and red dots represent the relative conductance of DPB-based materials and DPF-based materials, respectively. All values are normalized to the DPB-based materials. The conductance values are selected at –0.1 V for STM-BJ and EGaIn and –1 V for macroscopic measurements.

$Au^{A\text{-}DE}$ indicates the annealing of Au substrates after being directly evaporated), and statistically generated the Gaussian long-average value of J ($\log|J|$) versus bias (V) with the deviation referring to previous reports (60, 61). It was found that the current density of films fabricated by DPB is comparable to that of films fabricated by the DPB cage. In contrast, the current density of DPF cage thin films showed an improvement by about one order of magnitude in conductance over that of DPF films (Fig. 4 *B* and *C*). These results showed that the conductance of monolayer thin films evaluated by EGaIn agreed well with the trends observed in single-ligand/cage junctions. This suggests that the quantum interference effects in DPB and DPF ligands, either constructive or destructive, can further transfer to their monolayer thin films in a larger length scale (Fig. 4*D*).

We further measured the charge transport characteristics of these materials at the macroscopic scale by using the pellet samples for the DPB ligand, DPF ligand, and the DPB and DPF cages (*SI Appendix*, Fig. S26). The pellet of the DPB ligand showed current–voltage (I-V) curve similar to that from the DPF ligand pellet, while similar behavior was observed in the pellet samples made from the DPB cage and the DPF cage. These results were completely different from what was observed at the microscopic scale. Fig. 4*D* shows the comparison of the conductivity of these four materials measured at the macroscopic and microscopic scales and reveals that the QI has no more influence on the conductivity of the macroscopic pellets.

Theoretical Calculations. To understand the scaling of QI from the DPB and DPF ligands to their cages, we performed further theoretical calculations. We first optimized the geometries of these ligands and cages in the gas phase and between gold electrodes using SIESTA (62), an implementation of DFT. The best agreement between the experimental and theoretical junction length was obtained in the configurations (*SI Appendix*, Fig. S31*C*). Using the mean-field Hamiltonian obtained from converged DFT calculations, we computed the transmission coefficient $T(E)$ of electrons traversing from one electrode to the other through molecules using our quantum transport code, GOLLUM (63, 64). The electrical conductance G at room temperature can be then calculated using the Landauer formula (63) (see *SI Appendix*, section S7). The DPF cage shows higher conductance than the DPB cage for all energies between the HOMO-LUMO gap (see *SI Appendix*, section S5 and Fig. S29). Furthermore, our calculations show that the DPB cage has lower conductance compared to that of the DPB ligand while the DPF cage shows higher conductance than the DPF ligand around the DFT Fermi energy (Fig. 5*A*), and these results are in good agreement with our measurements. The DPB, DPF molecules and their corresponding cages are smaller than a typical size that occurs hopping transport in the molecular wires (65, 66). Furthermore, a good agreement between our experiment and our theory result based on phase-coherent tunneling indicates that the dominant transport mechanism is phase-coherent tunneling in our molecular junctions. In particular, while the length of DPF and DPB cages are almost the same, DPF cage shows nearly 1.7 orders of magnitude higher conductance than DPB cage (Fig. 2*C*). Our theory demonstrates that this is due to the QI effects, which is a typical signature of the phase coherent transport in molecular junctions at room temperature.

The theoretical Seebeck coefficients (*SI Appendix*, section S7) show the same trends as the experimental results (Fig. 5*B*), indicating there are LUMO transports in all these four junctions. To understand the mechanism, we first calculated the molecular orbitals for these structures. While the LUMO is extended over the single DPB and DPF ligands, it is degenerate and localized on the Pd atoms in the cages (*SI Appendix*, Fig. S30). It is more pronounced in DPB molecules than in DPF molecules (*SI Appendix*, Fig. S31). We hypostasize that the

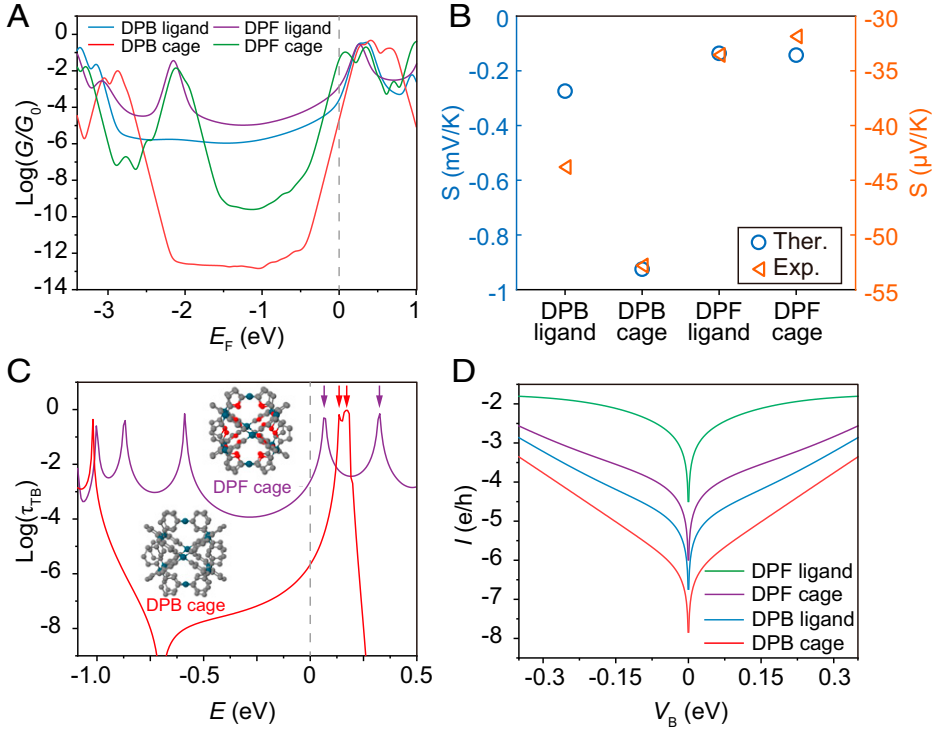

Fig. 5. Transport calculations of single-ligand/cage junctions. (*A*) Room temperature conductance versus electrodes Fermi energy obtained from DFT for DPB ligand (blue), DPB cage (red), DPF ligand (purple), and DPF cage (green). (*B*) Comparison of room temperature experimental and theoretical Seebeck coefficients of DPB ligands, DPB cages, DPF ligands, and DPF cages. (*C*) Transmission coefficient τ (E) for simple tight-binding (TB) model of structures shown in the *Insets*. (*D*) Current-voltage (*I-V*) relationship for DPB ligand, DPB cage, DPF ligand, and DPF cage. e is the electron charge and h is the Planck's constant.

transport around LUMO is through localized orbitals on Pd atoms (see local density of state in *SI Appendix*, Fig. S31 *C* and *F*) and ligand acts as an effective electronic coupling (γ) between Pd atoms as shown with a simple model in *SI Appendix*, Fig. S28. This effective coupling is weaker for DPB where transport is hampered by DQI and stronger for DPF where QI is constructive. Because of the Pd–Pd coupling, the QI effects featured in ligands can be transferred to the cages under a phase-coherent distance scale. As a consequence, the splitting of degenerate LUMO orbitals in the DPB cage due to Pd atoms is less than that in the DPF cage (*SI Appendix*, Figs. S28 and S30). It is also evident in tight-binding (TB) transmission coefficient calculations in a simple model using one orbital per atom (see details in *SI Appendix*, Fig. 5 *C*, *Inset*, and *SI Appendix*, Fig. S28). The splitting of degenerate LUMO levels is smaller in the DPB cage (red arrows) than in the DPF cage (purple arrows) where the splitting of LUMO levels is larger. Because of such larger splitting in the DPF cage, the LUMO resonance there gets closer to the Fermi energy and this leads to an improved conductance compared to that of the DPF ligand. This is not the case in the DPB cage because the splitting of LUMO resonances is smaller. The *I-V* characteristic of these junctions was also calculated. The overall shape of *I-V* curve for DPB and the DPB cage is similar because the LUMOs in the DPB ligand and cages are close to each other (Fig. 5*D*). In contrast, the *I-V* curve shows a sharper V shape in DPF cage for a small bias followed by the saturation of current by a higher bias in contrast to that of a single DPF molecule (Fig. 5*D*). This sharp V-shaped *I-V* curve for small bias and current saturation in the DPF cage also suggests that the LUMO is close to the Fermi energy and in agreement with the experiments.

Discussion

We reported the scaling of QI effects from organic ligands to the molecular cages and the monolayer thin film of these molecular cages. The single-molecule conductance of the DPF cage is ∼42 times of that of the DPB cage, while the conductance of a DPF ligand is only approximately nine times of that of a DPB ligand. Thermopower measurements indicate that the charge transport mainly occurs on the LUMO among all the single-molecule/cage junctions, and the Flicker noise analysis reveals the through-space transport for DPB ligand junctions and through-bond transport for DPF ligand junctions. It was experimentally and theoretically determined that the transport remains phase-coherent at the single-ligand scale, the single-cage scale, and the assembled monolayer scale. Such molecular cage, with 732 atoms, was the largest molecular system with QI effects in single-molecular junctions so far. Our work suggested that the QI could be scaled up within the phase-coherent distance, which is essential for the design of QI-based molecular electronic materials and devices. This work might be of interest to a broad audience across the areas of supramolecular chemistry, physical science, and material science.

Materials and Methods

Materials Synthesis. The DPB and DPF ligands were synthesized by a Suzuki coupling reaction according to previous reports (41, 67, 68). The $M_{12}L_{24}$ molecular cages were synthesized according to a previous report with slight modification (41). Specifically, the DPB or DPF ligand (0.005 mmol) reacted with Pd^{2+} (0.0025 mmol) stoichiometrically in deuterated dimethyl sulfoxide (d_6-DMSO) (1 mL) at 70 °C for 12 h to form the DPB cage or the DPF cage. The detailed synthesis procedures and characterization data are listed in *SI Appendix*.

Data Analysis Details. Conductance histograms were constructed from the conductance traces with a bin size of 1,000 (bin width = 0.01 $\log(G/G_0)$). Two-dimensional conductance-distance histograms were constructed with a bin size of 1,000 × 500 ($\log(G/G_0)$ × nm). The conductance-distance traces are aligned by taking $\Delta z = 0$ for the conductance value equal to $10^{-0.3}$ G_0.

Theoretical Calculation Details. The optimized geometry and ground state Hamiltonian and overlap matrix elements of each structure were self-consistently obtained using the SIESTA (62) implementation of the density functional theory (DFT). SIESTA employs norm-conserving pseudopotentials to account for the core electrons and linear combinations of atomic orbitals in construction of the valence states. The generalized gradient approximations (GGA) of the exchange and correlation functional is used with PBE parameterization, a double-ζ polarized (DZP) basis set, a real-space grid defined with an equivalent energy cutoff of 150 Ry. The geometry optimization for each structure is performed with forces smaller than 10 meV/Å. From the mean-field Hamiltonian obtained from DFT or simple tight-binding model, we calculate the electrical conductance and Seebeck coefficient (63, 64) (*SI Appendix*, section S7 for details).

Data, Materials, and Software Availability. Open-source code XME-data analysis data have been deposited in GitHub (https://github.com/Pilab-XMU/XMe_DataAnalysis) (69). All study data are included in the article and/or *SI Appendix*.

ACKNOWLEDGMENTS. We acknowledge the support from National Natural Science Foundation of China (21722305, T2222002, 21973079, 22032004, 21991130) and the Natural Science Foundation of Fujian Province (2021J06008). X.X. thanks the support from China Postdoctoral Science Foundation (2020M682082 and 2021T140396). H.S. acknowledges the UKRI for Future Leaders Fellowship (MR/S015329/2). S.S. acknowledges the Leverhulme Trust for Early Career Fellowship (ECF-2018-375). N.B. acknowledges the School of Engineering PhD studentship.

1. I. Stone *et al.*, A single-molecule blueprint for synthesis. *Nat. Rev. Chem.* **5**, 695–710 (2021).
2. J. Liu, X. Huang, F. Wang, W. Hong, Quantum interference effects in charge transport through single-molecule junctions: Detection, manipulation, and application. *Acc. Chem. Res.* **52**, 151–160 (2019).
3. Y. Li *et al.*, Transition from stochastic events to deterministic ensemble average in electron transfer reactions revealed by single-molecule conductance measurement. *Proc. Natl. Acad. Sci. U.S.A.* **116**, 3407–3412 (2019).
4. C. Jia *et al.*, Quantum interference mediated vertical molecular tunneling transistors. *Sci. Adv.* **4**, eaat8237 (2018).
5. R. J. Nichols, S. J. Higgins, Single molecule nanoelectrochemistry in electrical junctions. *Acc. Chem. Res.* **49**, 2640–2648 (2016).
6. D. Xiang, X. Wang, C. Jia, T. Lee, X. Guo, Molecular-scale electronics: From concept to function. *Chem. Rev.* **116**, 4318–4440 (2016).
7. T. A. Su, M. Neupane, M. L. Steigerwald, L. Venkataraman, C. Nuckolls, Chemical principles of single-molecule electronics. *Nat. Rev. Mater.* **1**, 16002 (2016).
8. D. Z. Manrique *et al.*, A quantum circuit rule for interference effects in single-molecule electrical junctions. *Nat. Commun.* **6**, 6389 (2015).
9. A. J. Heinrich *et al.*, Quantum-coherent nanoscience. *Nat. Nanotechnol.* **16**, 1318–1329 (2021).
10. Y. Liu, X. Qiu, S. Soni, R. C. Chiechi, Charge transport through molecular ensembles: Recent progress in molecular electronics. *Chem. Phys. Rev.* **2**, 021303 (2021).
11. Y. Yang *et al.*, Heteroatom-induced molecular asymmetry tunes quantum interference in charge transport through single-molecule junctions. *J. Phys. Chem. C* **122**, 14965–14970 (2018).
12. Y. Li *et al.*, Gate controlling of quantum interference and direct observation of anti-resonances in single molecule charge transport. *Nat. Mater.* **18**, 357–363 (2019).
13. M. Koole, J. M. Thijssen, H. Valkenier, J. C. Hummelen, H. S. van der Zant, Electric-field control of interfering transport pathways in a single-molecule anthraquinone transistor. *Nano Lett.* **15**, 5569–5573 (2015).
14. J. Bai *et al.*, Anti-resonance features of destructive quantum interference in single-molecule thiophene junctions achieved by electrochemical gating. *Nat. Mater.* **18**, 364–369 (2019).
15. J. P. Bergfield, H. M. Heitzer, C. Van Dyck, T. J. Marks, M. A. Ratner, Harnessing quantum interference in molecular dielectric materials. *ACS Nano* **9**, 6412–6418 (2015).
16. H. Vazquez *et al.*, Probing the conductance superposition law in single-molecule circuits with parallel paths. *Nat. Nanotechnol.* **7**, 663–667 (2012).
17. M. H. Garner *et al.*, Comprehensive suppression of single-molecule conductance using destructive σ-interference. *Nature* **558**, 415–419 (2018).
18. E. Maggio, G. C. Solomon, A. Troisi, Exploiting quantum interference in dye sensitized solar cells. *ACS Nano* **8**, 409–418 (2014).
19. C. Zhan *et al.*, Single-molecule plasmonic optical trapping. *Matter* **3**, 1350–1360 (2020).

20. S. Kanai *et al.*, Generalized scaling of spin qubit coherence in over 12,000 host materials. *Proc. Natl. Acad. Sci. U.S.A.* **119**, e2121808119 (2022).
21. M. Famili *et al.*, Self-assembled molecular-electronic films controlled by room temperature quantum interference. *Chem* **5**, 474–484 (2019).
22. S. Soni *et al.*, Understanding the role of parallel pathways via in-situ switching of quantum interference in molecular tunneling junctions. *Angew. Chem. Int. Ed. Engl.* **59**, 14308–14312 (2020).
23. C. R. Arroyo *et al.*, Signatures of quantum interference effects on charge transport through a single benzene ring. *Angew. Chem. Int. Ed. Engl.* **52**, 3152–3155 (2013).
24. C. E. McCold *et al.*, Molecular control of charge carrier and seebeck coefficient in hybrid two-dimensional nanoparticle superlattices. *J. Phys. Chem. C* **124**, 17–24 (2019).
25. J. E. Greenwald *et al.*, Highly nonlinear transport across single-molecule junctions via destructive quantum interference. *Nat. Nanotechnol.* **16**, 313–317 (2021).
26. S. Fujii *et al.*, Rectifying electron-transport properties through stacks of aromatic molecules inserted into a self-assembled cage. *J. Am. Chem. Soc.* **137**, 5939–5947 (2015).
27. M. Kiguchi *et al.*, Highly conductive [3×n] gold-ion clusters enclosed within self-assembled cages. *Angew. Chem. Int. Ed. Engl.* **52**, 6202–6205 (2013).
28. M. Kiguchi *et al.*, Electron transport through single molecules comprising aromatic stacks enclosed in self-assembled cages. *Angew. Chem. Int. Ed. Engl.* **50**, 5708–5711 (2011).
29. T. Brandl *et al.*, Iron in a cage: Fixation of a Fe(II)tpy$_2$ complex by fourfold interlinking. *Angew. Chem. Int. Ed. Engl.* **59**, 15947–15952 (2020).
30. C. Evangeli *et al.*, Engineering the thermopower of C60 molecular junctions. *Nano Lett.* **13**, 2141–2145 (2013).
31. M. W. Gu, H. H. Peng, I. P. Chen, C. H. Chen, Tuning surface d bands with bimetallic electrodes to facilitate electron transport across molecular junctions. *Nat. Mater.* **20**, 658–664 (2021).
32. Y. Lv *et al.*, Single cycloparaphenylene molecule devices: Achieving large conductance modulation via tuning radial π-conjugation. *Sci. Adv.* **7**, eabk3095 (2021).
33. S. Yuan, Q. Zhang, Application of one-dimensional nanomaterials in catalysis at the single-molecule and single-particle scale. *Front Chem.* **9**, 812287 (2021).
34. L. Lafferentz *et al.*, Conductance of a single conjugated polymer as a continuous function of its length. *Science* **323**, 1193–1197 (2009).
35. S. Ho Choi, B. Kim, C. D. Frisbie, Electrical resistance of long conjugated molecular wires. *Science* **320**, 1482–1486 (2008).
36. Y. Zang *et al.*, Cumulene wires display increasing conductance with increasing length. *Nano Lett.* **20**, 8415–8419 (2020).
37. H. Rascón-Ramos, J. M. Artés, Y. Li, J. Hihath, Binding configurations and intramolecular strain in single-molecule devices. *Nat. Mater.* **14**, 517–522 (2015).
38. B. Zhang *et al.*, Role of contacts in long-range protein conductance. *Proc. Natl. Acad. Sci. U.S.A.* **116**, 5886–5891 (2019).
39. B.-F. Zeng *et al.*, *In situ* lattice tuning of quasi-single-crystal surfaces for continuous electrochemical modulation. *Chem. Sci. (Camb.)* **13**, 7765–7772 (2022).
40. M. Elstner *et al.*, Self-consistent-charge density-functional tight-binding method for simulations of complex materials properties. *Phys. Rev. B* **58**, 7260–7268 (1998).
41. M. Tominaga *et al.*, Finite, spherical coordination networks that self-organize from 36 small components. *Angew. Chem. Int. Ed. Engl.* **43**, 5621–5625 (2004).
42. Q. F. Sun *et al.*, Self-assembled M24L48 polyhedra and their sharp structural switch upon subtle ligand variation. *Science* **328**, 1144–1147 (2010).
43. A. I. Yanson, G. R. Bollinger, H. E. van den Brom, N. Agraït, J. M. van Ruitenbeek, Formation and manipulation of a metallic wire of single gold atoms. *Nature* **395**, 783–785 (1998).
44. W. Hong *et al.*, Single molecular conductance of tolanes: Experimental and theoretical study on the junction evolution dependent on the anchoring group. *J. Am. Chem. Soc.* **134**, 2292–2304 (2012).
45. W. Hong *et al.*, An MCBJ case study: The influence of π-conjugation on the single-molecule conductance at a solid/liquid interface. *Beilstein J. Nanotechnol.* **2**, 699–713 (2011).
46. B. Huang *et al.*, Controlling and observing sharp-valleyed quantum interference effect in single molecular junctions. *J. Am. Chem. Soc.* **140**, 17685–17690 (2018).
47. M. Gantenbein *et al.*, Quantum interference and heteroaromaticity of para- and meta-linked bridged biphenyl units in single molecular conductance measurements. *Sci. Rep.* **7**, 1794 (2017).
48. O. Adak *et al.*, Flicker noise as a probe of electronic interaction at metal-single molecule interfaces. *Nano Lett.* **15**, 4143–4149 (2015).
49. D. Xiang *et al.*, Noise characterization of metal-single molecule contacts. *Appl. Phys. Lett.* **106**, 063702 (2015).
50. C. Tang *et al.*, Multicenter-bond-based quantum interference in charge transport through single-molecule carborane junctions. *Angew. Chem. Int. Ed. Engl.* **58**, 10601–10605 (2019).
51. A. Borges, J. Xia, S. H. Liu, L. Venkataraman, G. C. Solomon, The role of through-space interactions in modulating constructive and destructive interference effects in benzene. *Nano Lett.* **17**, 4436–4442 (2017).
52. P. Reddy, S. Y. Jang, R. A. Segalman, A. Majumdar, Thermoelectricity in molecular junctions. *Science* **315**, 1568–1571 (2007).
53. K. Baheti *et al.*, Probing the chemistry of molecular heterojunctions using thermoelectricity. *Nano Lett.* **8**, 715–719 (2008).
54. R. Miao *et al.*, Influence of quantum interference on the thermoelectric properties of molecular junctions. *Nano Lett.* **18**, 5666–5672 (2018).
55. M. Paulsson, S. Datta, Thermoelectric effect in molecular electronics. *Phys. Rev. B* **67**, 241403 (2003).
56. H. Chen *et al.*, Exploring the thermoelectric properties of oligo(phenylene-ethynylene) derivatives. *Nanoscale* **12**, 15150–15156 (2020).
57. S. Yuan *et al.*, Single-atom control of electrical conductance and thermopower through single-cluster junctions. *Nanoscale* **13**, 12594–12601 (2021).
58. Y. Hu *et al.*, Single dynamic covalent bond tailored responsive molecular junctions. *Angew. Chem. Int. Ed. Engl.* **60**, 20872–20878 (2021).
59. J. Shi *et al.*, The influence of water on the charge transport through self-assembled monolayers junctions fabricated by EGaIn technique. *Electrochim. Acta* **398**, 139304 (2021).
60. L. Yuan, L. Jiang, B. Zhang, C. A. Nijhuis, Dependency of the tunneling decay coefficient in molecular tunneling junctions on the topography of the bottom electrodes. *Angew. Chem. Int. Ed. Engl.* **53**, 3377–3381 (2014).
61. C. S. S. Sangeeth *et al.*, Comparison of DC and AC transport in 1.5-7.5 nm oligophenylene imine molecular wires across two junction platforms: Eutectic Ga-In versus conducting probe atomic force microscope junctions. *J. Am. Chem. Soc.* **138**, 7305–7314 (2016).
62. J. M. Soler *et al.*, The SIESTA method for ab initio order-N materials simulation. *J. Phys. Condens. Matter* **14**, 2745–2779 (2002).
63. H. Sadeghi, Theory of electron, phonon and spin transport in nanoscale quantum devices. *Nanotechnology* **29**, 373001 (2018).
64. J. Ferrer *et al.*, GOLLUM: A next-generation simulation tool for electron, thermal and spin transport. *New J. Phys.* **16**, 093029 (2014).
65. S. Park *et al.*, Thermopower in transition from tunneling to hopping. *Nano Lett.* **22**, 7682–7689 (2022).
66. X. Zhao *et al.*, Oligo(aryleneethynylene)s with terminal pyridyl groups: Synthesis and length dependence of the tunneling-to-hopping transition of single-molecule conductances. *Chem. Mater.* **25**, 4340–4347 (2013).
67. L. Zeng *et al.*, Hierarchical gelation of a $Pd_{12}L_{24}$ metal-organic cage regulated by cholesteryl groups. *Inorg. Chem.* **58**, 10019–10027 (2019).
68. C. Hua, D. M. D'Alessandro, Systematic tuning of Zn(II) frameworks with furan, thiophene, and selenophene dipyridyl and dicarboxylate ligands. *Cryst. Growth Des.* **17**, 6262–6272 (2017).
69. C. Shang *et al.*, Pilab-XMU / XMe_DataAnalysis. GitHub. https://github.com/Pilab-XMU/XMe_DataAnalysis. Deposited 15 December 2021.